Role of Pr on the Semiconductor Properties of Nanotitania. An Experimental and First-Principles Investigation

(Article begins on next page)

18 October 2024

UNIVERSITÀ DEGLI STUDI DI TORINO

The role of Pr on the semiconductor properties of nanotitania. An experimental and first principle investigation

Francesca Spadavecchia,[*,†] Giuseppe Cappelletti, [†] Silvia Ardizzone, [†] Michele Ceotto, [†] Matteo Simone Azzola, [†]Leonardo Lo Presti, [†,≠] Giuseppina Cerrato,[‡] Luigi Falciola[†]

[†] Dipartimento di Chimica, Università degli Studi di Milano, Via Golgi 19, 20133 Milano, Italy. Phone: +390250314219, fax: +390250314228

[≠] Istituto di Scienze e Tecnologie Molecolari, Italian CNR, Via Golgi 19, 20133 Milano, Italy

[‡] Dipartimento di Chimica & NIS centre of Excellence & INSTM-RU of Torino, Università degli Studi di Torino, Via P. Giuria 7 – 10125 Torino, Italy.

* To whom correspondence should be addressed: francesca.spadavecchia@unimi.it

ABSTRACT

Nanostructured Pr-doped titania samples were obtained in the 7-10 nm range starting from a classical sol-gel synthesis and the effects of the dopant on the semiconductor properties have been extensively studied. The materials, synthesized at various nominal Pr/Ti molar ratios (0.2, 0.3, 0.5, 0.7), were investigated by X-ray powder diffraction (XRPD), high-resolution transmission electron microscopy (HR-TEM), UV–Vis spectroscopy, N_2 adsorption–desorption isotherm, EDX analysis. A complete photoelectrochemical characterization was also carried out by means of photocurrent and photovoltage measurements. It was found that Pr doping induces high crystallinity and sometimes slows the recombination of photogenerated electrons and holes in TiO_2, modifying the absorption spectra with specific features in the visible region. The effects of the dopant on the band energy level, surface area, pore volume, crystal size of the $Pr-TiO_2$ samples were systematically investigated as well. The experimental picture was implemented by plane-wave bulk DFT calculations, that allowed us to reach a thorough and complete understanding of the energy states originating from the dopant in the bandgap and provided important insights into the interplay among structural and electronic degrees of freedom in the lattice. In particular, strong evidences emerge that the foreign Pr ion should be present as substitutional in the titania lattice and electronic photoexcitation enhancements are generated by the presence of f orbitals just below the conduction band. Therefore, nanostructured $Pr-TiO_2$

KEYWORDS

1. INTRODUCTION

A variety of TiO_2 nanostructured materials has been attracting increasing attention for both academic wide material characterization and specific applications, such as photocatalysis,[1-3] solar cells,[4-6] and sensors.[7,8] An astounding number of publications can be found in the literature about titania not only synthesized in various sizes and shapes but also structurally modified, showing that doping a wide-band-gap semiconductor with metal and non-metals leads to substantial changes in its specific electronic features (apparent band gap narrowing) and physical properties.[9,10]

In addition to the main drawback of titanium dioxide, due to its quite large intrinsic bandgap (3.0-3.2 eV), a second important issue to be controlled and optimized is the low quantum photoefficiency due to the high recombination rate of photogenerated electron–hole (e_-–h_+) pairs.[11] This is a recurring problem during photoelectrochemical and photocatalytic processes, and it is often considered to some extent the major limitation for TiO_2 widespread applications.[12] Unfortunately, the recombination of photogenerated charge carriers most often results to be an undesired effect of the modifications made on titania to overcome the wide bandgap issue and the related visible light inactivity. If, on the one hand, the presence of transition metal centers in TiO_2 leads to a considerable bandgap red-shift towards the light absorption, on the other hand these centers, which are commonly considered as impurities or traps, may act in some cases as recombination centers for electrons and holes, thus reducing the overall activity of the photocatalyst.[13]

While the number of papers on p-block non-metal dopants (especially B, C, N) has undergone an exponential increase, some other promising heteroatoms are very scantily taken into account.[14-16] In this respect, rare-earth (RE) metals have started to show a tremendous potential improvement of several TiO_2 features, becoming interesting sources for new advanced materials and receiving quite much attention as dopants too. It is reported that doping TiO_2 with such metal ions[17-21] can slow the recombination rate of photogenerated charge pairs by shallowly trapping electrons and enhance the interfacial charge transfer efficiency due to the ability of the metal to form complexes with a Lewis base (e.g., amines, aldehydes, alcohols, thiols, etc.) via interactions of functional groups of the base with the metal empty f-orbitals.[15] Secondly, the RE dopant can retard the transformation from anatase to rutile phase[18] and also inhibit the increase of the crystallite size.[14]

Consequently, Pr-TiO$_2$ systems may find successful applications in photocatalysis, as already pointed out by several authors both recently and in the past.[14,21-23]

However, no complementary experimental and theoretical studies have been found in the literature focusing on the above mentioned aspects: only a detailed paper about Pr-CeO$_2$ dealt with the structural differences between doped and undoped oxides from the theoretical point of view.[24] In another study, Chen et al. analyzed the electronic structures of the different lanthanide-doped systems by using a DFT + U (Density Functional Theory with Hubbard U correction) approach:[25] the bulk dopants substitutional energies were computed whereas band structures and partial density of states (PDOS) were compared with that of pure anatase TiO$_2$. These theoretical calculations corroborated the electronic and structural experimental results. A similar combined approach was employed in our previous work concerning the location of nitrogen dopant species in TiO$_2$ matrix.[26]

In this work, we aimed at focusing on a synergic and deep experimental and theoretical characterization of Pr-doped TiO$_2$ from both electronic and structural points of view, while keeping the synthetic strategies as simple, quick and effortless as possible. We synthesized Pr-doped titania samples by a classical sol-gel route, with the emphasis placed upon single metal doping and Pr as a representative RE element. Then, amperometric electrochemical measurements pointed out that the charge recombination rate is reduced by doping. Also, the presence of the heteroatom clearly modifies the diffuse reflectance spectra (DRS) of the oxides with specific features in the visible region. These two experimental findings not only witness TiO$_2$ doping has occurred, but also prove that the final materials definitely got some benefit from the presence of praseodymium.

By placing theory and experiment side by side, we aimed at systematically and fully explore this system to gain novel insights into the interplay among structural and electronic degrees of freedom that underlie the observed photochemical properties of this fascinating material.

2. EXPERIMENTAL AND COMPUTATIONAL SET-UP

2.1. Synthesis

TiO$_2$ precursor was obtained by acidic hydrolysis (pH 4 by adding HCl) of titanium(IV) isopropoxide in 2-propanol at room temperature. Except for a reference undoped sample (named "T"), a varied amount of Pr(NO$_3$)$_3$ (Pr/Ti = 0.2-0.3-0.5-0.7 % molar ratio) was dissolved in the aqueous HCl solution, which was

added dropwise to the organic mixture. The colloidal suspension was stirred at 300 rpm for 90 minutes and then dried in the oven at 80 °C overnight. Finally the dry powder was calcined at 400 °C under oxygen stream. Doubly distilled Milli-Q (Millipore Corporation) water was used and reagent grade chemicals were supplied by Aldrich. Doped titania samples were named "TPr_x", with x standing for the percentage of initial Pr/Ti molar ratio.

2.2. X-ray powder diffraction experiments

X-ray powder diffraction (XRPD) experiments were performed on the freshly prepared nanostructured TiO_2 samples to evaluate the amount of their brookite content and possible changes in the lattice parameters, crystallite size and lattice strain as a function of the doping extent. The diffraction profiles were recorded at room temperature by a Philips PW 3710 Bragg-Brentano goniometer equipped with a scintillation counter and 1° divergence slit, 0.2 mm receiving slit and 0.04° soller slit systems. We employed graphite-monochromated Cu Kα radiation at 40 kV x 40 mA nominal X-rays power. The same data collection strategy was applied to all the specimens. More in detail, we performed ∇:2∇ scans between 20° to 90°, with step size 0.08° wide, for a total counting time of 4 hours. A microcrystalline Si-powdered sample was used as a standard to correct for instrumental line broadening effects. The XRPD patterns were analyzed with the Rietveld method as implemented in the GSAS-EXPGUI program suite.[27,28] The background was described by power series in $Q_{2n}/n!$ and $n!/Q_{2n}$ and a surface roughness correction for microabsorption effects was also applied.[29] Line profiles were fitted using a pseudo-Voigt function.[30] Preferred orientation of crystallites was taken into account by a spherical harmonic model.[31] In the last cycles of the refinement, scale coefficient(s), cell parameters, positional coordinates and thermal factors were allowed to vary, as well as background and profile coefficients. All the attempts made to exactly locate the Pr ions in the unit cell from the experimental XRPD patterns were unsuccessful, probably because the low doping extent and the inherently disordered nature of the dopant ions. In any case, in accordance also with our HRTEM and literature results,[32] no evidence of Pr segregation was detected anyway (see also the discussion below). The complete list of agreement factors of the various fittings, together with the final structural models at convergence, can be found within the Supporting Information (Tables S1 and S2).

2.3. Electrochemical analysis

The electron-hole recombination processes of pristine and doped TiO_2 films was studied by measuring the photocurrent transients developed by irradiating the photoanode (TiO_2) with UV light.[33] The photoelectrochemical cell was a three compartment one, with two counter electrodes, both consisting in a Pt wire parallel to the working electrode, a saturated calomel electrode as reference, a Luggin capillary in order to minimize the ohmic drop and a TiO_2 film located in the middle of the cell as working electrode. An aqueous electrolyte (0.5 M NaCl, spontaneous pH) was used. The photoanode was alternatively exposed to UV light, generated by a 500 W UV halogen lamp (Jelosil HG 500, iron halides, 85 mW effective power), emitting in the 315-400 nm wavelength range, and the photocurrent was measured by a microIII Autolab potentiostat/galvanostat (EcoChemie, The Netherlands).

Preliminary linear sweep voltammetry analyses were recorded in the same experimental conditions at a scan rate of 50 mV s^{-1} to evaluate the potential at which the photocurrent was constant to be chosen (as working potential) for the chronoamperometric tests. The photocurrent-time behavior under constant electrode polarization was then obtained with hand-chopped light. Before recording the transient, the applied potential was kept constant in the dark in order to establish dark current equilibrium and nitrogen was flown into the cell. All measurements were performed under nitrogen flow and in the dark, since the indoor light gives a positive background current. After the photoanodes reached the open-circuit equilibrium, the electrodes were exposed to light for 200 s. During this time the closed-circuit current transient was recorded. A 100 s dark exposition followed after a new exposure to light. The dark/light alternation was repeated for at least 6 times, in order to obtain reproducible transient patterns.

The working electrode was a TiO_2 thin film prepared by spin-casting a 2-propanol suspension of the oxide powder with a Spin150 spin-coater (SPS, ATP GmbH) onto flourine-doped tin oxide (FTO) conducting glass (Aldrich, 2.3 mm thick, ~7 /sq surface resistivity). The suspension was drop-cast on the substrate and spun at 2000 rpm for 20 s, using a scotch tape as a frame in order to have an active area of 3 cm_2 and the deposition was repeated for 8 layers. The as-prepared films were finally sintered at 400 °C in air for 1 h.

The quasi-Fermi level of electrons was measured using methylviologen dichloride ($(MV)Cl_2$, E_{red} (MV_{2+}/MV_{+})= - 0.4421 V vs NHE) as a pH-independent redox system, according to the literature.[34] Here the semiconductor powder was directly used as suspension in the electrolyte (KNO_3, 0.1 M aqueous solution), with the operative procedure and experimental setup described in a previous work.[35] Stable photovoltages

were acquired by irradiating the (Pr-)TiO$_2$ suspension with the UV lamp mentioned above for the photocurrent tests.

2.4. Other experimental measurements

Optical measurements in the UV-visible range were performed using a Perkin-Elmer, Lambda 35 spectrophotometer, equipped with a diffuse reflectance accessory.

Specific surface areas and pore volumes were determined by the classical BET-BJH procedure using a Coulter SA 3100 apparatus.

HR-TEM investigations were carried out employing a JEOL 3010-UHR instrument (300 kV acceleration potential; LaB$_6$ filament) equipped with an Oxford INCA X-ray energy dispersive spectrometer (EDS) with a Pentafet Si(Li) detector. Samples were ''dry'' dispersed on lacey carbon Cu grids.

2.5. Computational details

Spin-polarized calculations were performed within the Generalized Gradient Approximation (GGA)[36] to Density Functional Theory (DFT)[37,38] with the Perdew–Burke–Ernzerhof (PBE) exchange correlation functional.[39,40] The Kohn-Sham scheme was solved using the plane wave basis with projected augmented wave method (PAW)[41,42] implemented in the Vienna Ab-initio Simulation Package code (VASP),[43,44] with an energy cutoff of 400 eV. The ground state optimizations were obtained by minimizing the partial derivatives of free energy with respect to the atomic position, including the Harris-Foulkes correction to forces,[45,46] using the conjugate-gradient scheme.[47,48] Iterative relaxation of atomic positions was stopped when the change in total energy between successive steps was less than 0.001 eV. Electronic property calculations were carried out using the block Davidson scheme.[49] The supercell and atomic relaxations were carried out until the residual forces were below 0.01 eV/Å. The bulk doped systems were constructed from the relaxed 3x3x3 162-atom anatase TiO$_2$ supercell. Reciprocal space sampling was restricted to the Γ-point, which is justified due to the rather large size of the used simulation supercells. Given the nature of the atoms considered and to properly describe the reduced Ti ions, we have applied the GGA+U method, formulated by Dudarev et al.,[50] to account for the strong on-site Coulomb repulsion amid the localized Ti 3d and Pr 4f electrons. Comparison with UPS (ultraviolet photoelectron spectroscopy) data suggested a value of U = 3eV.[51] However, there is no agreement on a precise value of U for all oxidation states of Ti, and the values of U span a range from 2 to 8 eV, as a result of the U dependence on the oxide, the Ti oxidation states, and the

underlying exchange-correlation functional.[52-56] Theoretical calculations for catalysis showed that U values can also be derived from the oxidation of Ti_2O_3 to TiO_2 reaction energy and one should prefer using either PBE+U or PW91+U, with U =2-3 eV.[57] Finally, it is possible to adopt a self-consistent linear response approach for the determination of the Hubbard U correction term.[58,59] Mattioli *et al.*[60] found a value of 3.23 eV for the anatase Ti 3d electrons using this approach. In conclusions, these and other studies[51,55,61] provided evidence of the unsuitability of exchange-correlation functionals for describing the reduced Ti ions. Consequently we chose to perform our calculations with the U = 3 eV, 3.3 eV, 4 eV and 5 eV. As far as the U value for the 4f Pr orbitals, there have been several theoretical works to study the effects of lanthanide doping into titanium dioxide by first- principles calculations.[62,63] According to experiments,[64,65] Pr_2O_3 is a dieletric material with band gap energy equal to 3.9 eV. We simulated the Pr_2O_3 electronic structure with U = 0-1-2-3-4 eV and found the band gap to be, respectively, 3.81-3.85-3.94-4.03-4.12 eV. The 4f Pr electrons U value was then fixed to 2 eV.

The optimized undoped stoichiometric supercell lattice parameters were a=11.547 Å and c=16.472 Å (a=3.849 Å and c=9.535 Å for a primitive cell), in good agreement with experimental results.[66]

3. RESULTS AND DISCUSSION

To investigate any significant difference in the recombination times of Pr-doped and undoped titania, the morphological, structural, optical and electronic features of the same samples were analyzed.

The praseodymium dopant at different molar ratio (0.2-0.7 Pr/Ti initial amount) was introduced into the titania precursor by a synthesis which is typically a bulk procedure. EDX analyses confirmed the presence of the Pr species and the relative concentration in the titania powders (0.18-0.62 Pr/Ti atomic ratio). Moreover, Pr could be considered randomly present in both anatase and brookite TiO_2 polymorphs and its manifest effect also lies in a progressive increase of the average lattice distortion (see infra).

3.1. Morphological and structural characterizations

To shed some light on the external habit of the various TiO_2-based materials under study, both conventional transmission electron microscopy (C-TEM) and high-resolution transmission microscopy (HR-TEM) have been resorted to. The main features exhibited by the materials are summarized in Fig. 1: it can be observed that, despite the presence/absence of Pr, all samples show rather small particles, with average crystallites sizes in the 7-10 nm range, highly packed but also highly individual (see the three left-hand images, referring

to a low magnification investigation). If we inspect in more detail the ultimate morphology exhibited by the crystallites, we can evidence that, in the absence of Pr species, the plain TiO_2 particles (Fig. 1a) possess (i) roundish but highly defective edges and (ii) high crystallinity (as witnessed by the presence of both fringe and thickness (Moirè's) patterns):[67] the crystal planes which generate this feature are in the majority of the cases due the (101) crystal planes of the TiO_2 anatase polymorph. When Pr species are present (Fig. 1b,c), the overall features above described remain almost unchanged, in particular for what concerns both phase and family of planes most exposed, but for the edges: for both Pr-doped materials it can be evidenced a more regular shape of the crystallites, with slightly less defectivity. In no cases either the presence of segregated Pr-rich phases or the formation of rutile-rich phases has ever been observed.

As concerns the specific surface areas, those of Pr-doped samples are lower than that of the undoped oxide, being reduced by even one third for the sample with the highest Pr content (see Table 1, 2_{nd} column). Moreover, no specific linear trend occurs at increasing the Pr content. Accordingly, a substantial loss of the total pore volume is found with respect to the undoped TiO_2. Then, most of the survived pores are micropores (with the diameter lower than 6 nm), as reported in Table 1. This is in absolute accordance with Yana et al., who affirmed that all doped samples show a conspicuous percentage of micropores, with a quite sharp and narrow distribution.[68] In the Supporting Information the hysteresis loop of one doped sample is compared with that of the undoped one (Fig. S1). The lowering of the specific surface areas could be in accordance with a less prominent presence of defects, thus leading to less favorable charge recombination events, which resemble the chronoamperometric results (see section 3.3. below).

Figure 2 shows the diffraction patterns collected on the nanostructured TiO_2 powders at various doping extent, together with the corresponding least-squares fitting results. The significant intensity changes among different XRPD patterns (see, for example, the peak at < 25.5° in each diffractogram of Figure 2) were attributed to the effect of the preferred orientations of crystallites. All the specimens are clearly biphasic, as the large peak at 2ϑ H 30.8° is entirely due to the (211) reflection of brookite. However, the anatase structure appears to be the predominant one in all the diffractograms. No other phases were detected: attempt to add the rutile[69] or the Pr_2O_3 structures[70,71] to the model invariably led to the worsening of the least-square fit. As a matter of fact, most papers report the anatase phase as the only one found in rare-earth-doped TiO_2,[15,23,21,72] therefore corroborating the lacking of any detectable segregated Pr-based phase also in our

samples. The sole exception is represented by Amlouk *et al.* who synthesized transparent xerogel monoliths and detected traces of the $Pr_4(Ti_9O_{24})$ phase.[73] However, Amlouk *et al.* employed a very different procedure (the monoliths grew in 90 days and underwent a very high calcination temperature, 1200 °C) compared to the classical sol-gel route we followed, which was also used by the authors of the other cited papers.

As concerns our compounds, no clear trends are detectable in the cell parameters of both the anatase and brookite phases as a function of the Pr doping (see Table S3 in the Supporting Information), as their changes are non-monotonic and barely significant in terms of the corresponding estimated standard deviations. Moreover, the brookite content was found to be invariant throughout the whole sample series (see Table S4 in the Supporting Information). More in details, the weight fractions of anatase and brookite were estimated from the refined phase fraction coefficients to be, on average, as large as 0.612(1) and 0.388(1), respectively. The full width at half maximum (FWHM) values, corrected for the instrumental line broadening, of some representative reflections belonging to the anatase structure are shown in Figure 3a. Brookite reflections (not shown) exhibit an analogue behavior. Interestingly, as the nominal Pr/Ti molar ratio is increased, the diffraction profiles systematically broaden. Such an effect may provide information on the behavior of the lattice strain and the average crystallite sizes as a function of the doping extent. It should be noted, however, that these quantities are quite difficult to be computed when, as in the present case, the diffraction patterns suffer of significant peak superposition (for example, see Meneghini *et al.*[74]). We therefore chose to provide a couple of size-strain estimates from two well-routed methods that face the problem from different perspectives.

First of all, we applied the Williamson-Hall recipe[75] to the reflections belonging to the anatase structure up to $2\vartheta = 60°$. The corresponding linear least-squares fitting results are listed within the Supporting Information (Figure S2 and Table S5). From Figure 3b it can be seen that the average volume-weighted domain size, <D_V>, undergoes a < 16 % roughly linear reduction on going from the undoped sample (Pr/Ti = 0.0 %) to the most doped one (Pr/Ti = 0.7 %). In general, it should be noted that the XRPD estimates for the crystallite dimensions agree quantitatively with the HRTEM outcomes commented above, providing a further evidence of the very high crystalline nature of our nanostructured compounds. On the other hand, the average lattice strain parameter, Σ, undergoes a significant increase on going from the pure nanostructured TiO_2 to the doped specimens (Figure 3b)). It should be noted that Σ (TPr_0.2) H Σ (TPr_0.3) within 3 estimated standard

deviations, i.e., the apparent decrease of Σ upon going from the $Pr/Ti = 0.2\%$ sample to the 0.3% one is poorly significant from a statistical viewpoint.

Secondly, we employed the double-Voigt method[76,77] implemented in the program BREADTH.[78] Within this approach, the Lorentzian and Gaussian size and strain contributions to the physical profile broadening are singled out, provided that at least two reflections belonging to the same crystallographic family are analytically modelled with known suitable functions. In the present case, we employed three reflections of anatase, namely the (101), (202) and (303) ones, approximating their experimental line profile with pseudo-Voigt functions, whose FWHM (amplitude) and $|$ (mixing) parameters were retrieved from the optimized GSAS profile coefficients.[27] In this way, we were able to estimate the corresponding volume-weighted column length and strain distributions as a function of the real-space distance along the scattering vector, upon the assumption that the crystallite size distribution is lognormal (see Figure 3c and 3d). Some estimates for $<D_V>$ and $<\Sigma^2>_{1/2}$, based on such distributions, can be found within the Supporting Information (Figure S3). It should be stressed that the integral breadth-based methods, including the Williamson-Hall approach, only give the volume-weighted domain size and the upper limit of the microstrain.[79] On the contrary, the knowledge of the crystallite distribution, although being based on some (reasonable) a priori assumptions, is required to fully characterize the sample microstructure.[80] As concerns the present case, the results provided by the double-Voigt approach agree well with the conclusions above sketched on the basis of the Williamson-Hall method. More in detail, it can be seen that an increment of the dopant concentration implies the shift of the most probable value of the size distribution (the mode) towards lower values, i.e. it implies the corresponding reduction of the average crystallite size. At the same time, a progressive increment of the lattice strain can be also detected, with Σ (TPr_0.7) H Σ (TPr_0.5) > Σ (TPr_0.3) H Σ (TPr_0.2) > Σ (T) at equal L.

In conclusion, it can be stated that the increment of the lattice strain observed by both the methods correlates with the increasing amount of Pr, as the brookite content remains the same throughout the sample series here considered. Together with the lacking of segregated Pr-based phases in our compounds, this evidence implies that the RE ions are likely disorderly dispersed in the bulk matrix, being either in the octahedral interstitial sites or the substitutional positions of anatase TiO_2. At the same time, the average crystallite size tends to become a little smaller as the Pr concentration is increased, in agreement also with previously

reported literature results on nanostructured Pr-TiO$_2$ systems.[14] In any case, both the Williamson-Hall and the double-Voigt methods provide an estimate for this quantity in good agreement with the HRTEM outcomes.

As the diffraction experiments are not conclusive from the perspective of locating the Pr site within the TiO$_2$ lattice, we performed a plane-wave DFT geometric optimization of a bulk Pr-doped 3x3x3 supercell to understand if the XRPD outcomes are compatible either with substitutional or interstitial doping. We chose a supercell composed of 27 primitive cells, to reproduce the averaged cell distortions that can be observed by XRPD analysis. In other words, we looked at the distortion effects on the averaged cell parameters. The values of the cell anatase parameters after distortion, i.e,. a, b, c, and of the averaged primitive cell volume, are reported in Fig. S4. All the parameters increase under substitutional doping given the bigger effective ionic radius of Pr$_{3+}$ (0.99 Å) with respect to Ti$_{4+}$ (0.61 Å).[81] Nevertheless, these changes are more evident in the case of interstitial doping. To quantify the primitive cell distortion under doping, we introduced the distortion parameter $d = 2$ (a-b) / (a+b), where a and b are the primitive cell parameters obtained as an average over all the primitive cells considered in the simulation. If the primitive cell angles had been unchanged under doping, this parameter would have been the orthorombic cell distortion parameter. In our case, the angle changes are contained within 0.1°, and d is very similar to the orthorombic one. In Fig. 4 the values of d are reported for the undoped supercell in the presence of an oxygen vacancy (TiO$_2$+V$_O$), for the Pr substitutional doped supercell (TiO$_2$+V$_O$+Pr$_{sub}$) and for the interstitial Pr doped supercell (TiO$_2$+V$_O$+Pr$_{int}$). While substitutional doping leaves the d parameter unchanged, this is no longer true when the interstitial doping is considered. Thus, it would have not been possible to fit accurately interstitial Pr doping XRPD data with the anatase crystallographic model. Instead, as described above, our XRPD data fit with good statistical accuracy into the anatase model. Moreover, theoretical results do not depend significantly on the U value and the same conclusions can be reached for any U.

All these geometric considerations have been done on the averaged cell. In order to have a local insight, Table S6 reports the distances between the Ti or Pr atom and the O atoms placed at the octahedron vertexes. These distances do not change for different U values in the case of the Ti central atom. Instead, minor differences can be seen in the case of Pr. Specifically, for each U value, the Pr centered octahedron presents

slightly elongated distances by still keeping the octahedral shape. This view of the substitutional doping is compatible with the XRPD patterns previously discussed.

As a general remark, it should be stressed that, when DFT+U methods are employed to study the positions of dopant-induced defect states in a metal oxide, extreme care must be taken when making even qualitative conclusions without reference to more accurate approaches or experiments.

3.2. Optical and electronic characterizations

As already noticed by Xu et al., the presence of RE_{3+} ions in the TiO_2 matrix may lead in general to a red-shift of the O 2p to Ti 3d charge transfer band.[23] Indeed, when the dopant content is increased, a slightly more pronounced absorption in the visible region is obtained for all our doped samples (Fig. 5), with the presence of some peculiar absorption features. In the literature, Li et al.[21] reported that neodymium dopant did not significantly shift the main absorption band edge, but brought some new absorption peaks attributable to 4f internal electron transitions in the visible region. It was further confirmed that significant photoluminescence emission occurred in the visible range of 350-700 nm; this is likely due to the electron transfer between Nd_{3+} and TiO_2 owing to introduction of a Nd 4f level.[82] Compared to the undoped sample having a bandgap of 3.2 eV, all the doped ones have an apparent bandgap about 3.0 eV, according to the Kubelka–Munk equation.[83]

It should be noted that the photoexcited states of lanthanide ions attributed to 4f-5d or f-f transitions could transfer their excess energy to other molecules adsorbed to the semiconductor surface. These "host/guest" energy and electron transfer processes, on the other hand, should be a vital route in suppressing the recombination of charge carriers, thus playing a beneficial role in photocatalytic reactions.

To verify whether a shift of the conduction band edge is responsible for the decrease of the apparent bandgap energy, the position of the quasi-Fermi level ($_nE_f*$) was determined by measuring the photovoltage as a function of the suspension pH. A detailed description of the experimental settings can be found elsewhere.[35]

With this technique, a titration curve is obtained having the inflection point at that pH value (pH_0) at which the redox potential of a selected redox couple (methyl viologen) and the quasi-Fermi level of the oxide are equal. From pH_0, the quasi-Fermi level can be calculated for any pH value according to the following expression:

$$^nE_F^* (pH) = E_{red} (MV_{2+}/MV_+) - k(pH - pH_0) \qquad (1)$$

The values calculated for all samples are reported in Table 1, 7_{th} column. It can be noticed that the quasi-Fermi levels are only slightly shifted away from the conduction band of the oxide.

These data were compared with electronic DFT computations: we calculated the Fermi and quasi-Fermi (the first excited Kohn-Sham orbital) energy levels variation under Pr doping. From Fig. S5, one can observe there is not a unique answer for Fermi energy shift under substitutional Pr doping, but it depends on U values. Instead, the interstitial Pr doping shifts the Fermi energy level toward the conduction band edge for any U value.

However, during a photovoltage experiment, it is the quasi-Fermi energy level to be populated under irradiation and to be measured. Only as an approximation, the Fermi is assumed at the same level as the quasi-Fermi one, given that TiO_2 is a n-type semiconductor. For this reason, we plotted on the lower panel of Fig. S5 the quasi-Fermi energy variation under doping, finding a common trend for any U value for both doping sites. When a substitutional Pr doping is performed, the quasi-Fermi levels are lowered with respect to the conduction band, while when an interstitial doping occurs, the quasi-Fermi levels are raised toward the conduction band.

Given the experimental photovoltage observations, we can exclude once more the presence of substitutional Pr doping on our samples. The quasi-Fermi energy levels shift originated by substitutional Pr doping also confirm the apparent band gap narrowing observed by the Kubelka-Munk transformed DRS data.

To perform a closer comparison between experimental data and theoretical calculations, we plot in Fig. 6 the density of electronic states (DOS) of the doped supercell arrangements. In all panels the total spin polarized DOS of the Pr doped oxygen defected TiO_2 are reported in continuous black and dashed red curves. The Fermi energy is indicated by the vertical dashed line. As far as the Pr electrons are concerned, the d and f DOS have been magnified 10 times and put into evidence because these are located in the proximity of the valence and conduction bands. More specifically, in the case of substitutional doping (left panel of Fig.6) and for U>3 eV, the d states (blue curves) are located just above the valence band and they are filled, while the f orbitals (green curves) are just below the conduction band and they are empty. Small deviations are seen by varying the U value between 3,3 eV and 5 eV, while for U = 3 eV the Pr d orbitals place as mid-gap states. Instead, for Pr interstitial doping (right panel of Fig.6), the d and f orbitals generate a set of mid-gap states,

whose location vary with the value of U. Interestingly, these mid-gap f orbitals are filled, since Pr is not employed in any bond.

From this electronic description, we can infer that electronic transitions can occur from either filled d Pr orbitals or the valence band states to empty f orbitals just below the conduction band in the case of substitutional Pr doping. Instead, with the interstitial Pr doping set-up, the possible electronic transitions are from either d or f filled Pr orbitals to Ti 3d ones, which delimit the bottom of the conduction band. On the basis of the DRS results, that put into evidence the f orbitals contribution to the absorption, we can safely conclude that substitutional Pr doping should be preferred.

3.3. Photocurrent measurements

It is well known that the application of TiO_2 as a mutual photocatalyst for environmental remediation is based on its semiconductor properties, which need several experimental approaches to be properly described. To the best of our knowledge, no photoelectrochemical properties of the Pr-doped materials were reported, although they are of basic importance when studying photocatalysis. We studied the charge recombinations by photocurrent kinetics curves.[84] The chronoamperometric data show an immediate photoresponse consisting in an initial anodic spike, caused by the separation of photogenerated electron–hole pairs at the semiconductor/electrolyte interface, followed by an exponential decrease of the photocurrent with time. This can be ascribed to the holes that, after reaching the semiconductor surface, accumulate and recombine with electrons from the conduction band.[84]

By defining D as

$$D = \frac{I_t - I_{st}}{I_0 - I_{st}}$$

(2)

the photocurrent transient is given by the following kinetic equation

$$D = e^{t/\tau}$$

(3)

In the above expressions, I_t is the current at time t, I_{st} the stationary current, I_0 is the highest current obtained when the light is turned on, and τ is the transient time constant. Thus, the slope of the plot ln(D) vs time is the reciprocal of τ, which gives indications about the time for charge recombination processes in the films and is related to the mechanism of electrons flow, as an average between separation and recombination of electrons and holes. The higher the transient time constant, the more recombination processes are inhibited. In the

following, the numerical value of τ is extracted by at least three transient peaks (from 700 to 1550 s), and an average value is given for each sample.

The shape of the curves of the different samples is comparable except for the absolute values of the photocurrent maxima, as shown in Fig. 7a (sample TPr_0.3 as a representative one). Nevertheless, the decays of the photocurrent within a few seconds are steeper in the case of the undoped oxide, meaning that this sample is more affected by recombination of the photogenerated charges. Surprisingly, such an effect is just the result obtained when incorporating foreign ions into the TiO_2 lattice,[85] given the formation of defects sites. The presence of points defects (such as oxygen vacancies) and their predominance in a specific type of TiO_2 sample[26] could not be a priori supported. Fig. 7b shows a comparison between sample T (undoped titania) and TPr_0.3 as for ln(D) vs time plot. The linear behavior[84,86] indicates that the decay mechanism should be only due to surface recombination, leading to a first-order kinetics in electrons surface concentration; the same functional behavior seems to occur for all the samples tested, though it is more evident in the case of the undoped one. The transient time constants reported in the inset of Figure 7b for the doped samples are greater (18-25 s) than both that of the undoped sample (15 s) and most of those observed for compact single-crystal or polycrystalline titania electrodes in the literature.[84,87]

About this issue, it must be said that the shape of the photocurrent transients and the time constants themselves could be strongly affected by several parameters such as the concentration of the electrolyte, the presence of a certain hole acceptor, the light-dark cycles duration, and so on.[88,89] They all play an important role on the local concentration of electrons/holes acceptors. However, this dependence is not problematic for our purpose since we are interested in a comparison among a series of samples, keeping constant all experimental parameters.

Eventually, the chronoamperometric measurements suggest that the Pr-doped titania can either favor charge separation or suppress recombination processes or give both such effects. In this respect, they could be considered promising materials for photocatalytic remediation.

4. CONCLUSIONS

In conclusion, by means of a very quick and simple chemical route, Pr-doped titania nanocrystals in the 7-10 nm range were obtained. The effects of the RE ion doping on the band energy level, surface area, pore

volume, crystal size, DFT+U geometries and electronic structures of the Pr-TiO$_2$ samples were systematically investigated.

From the optical experimental results we found that Pr doping significantly modifies the DR spectra (see Fig. 5) of the final material and improve electron-hole separation, increasing the estimated τ. However, the reason of this enhancement was initially not clear and a debate could be opened on several factors, such as the chemical nature of the doping centers, their role on the band structure modifications of the solid and, consequently, the mechanism of photoactivation.

Only after the electrochemical and structural measurements performed in this work, complemented by periodic DFT calculations, we have been able to have a complete understanding of photoelectrochemical features and performances.

Specifically, by comparing DFT and DRS results, we deduced that Pr atoms are hosted in a Ti substitutional fashion within our samples. In this case, the visible light absorption enhancement is due to electronic transitions from valence band states or shallow d Pr orbitals to the f Pr empty orbitals just below the conduction band, as represented on the left panel of Fig. 6. We needed to set the DFT U parameter at values greater than 3 eV in order to reproduce such optical absorption experimental results. From a purely structural perspective, theoretical calculations suggest that the dopant ions introduced into the TiO$_2$ lattice could be mainly located as substitutional for titanium, since no major structural effects are obtained by substitutional doping versus the interstitial one, in agreement with the XRPD analysis.

Since the generated mid-gap levels are finally 4f states, and their location is quite close to the conduction band, the above mentioned electron transitions could easily happen, causing the absorption peaks in the visible region detected by the optical measurements of diffuse reflectance.

On the contrary, it has been computationally found that the presence of localized mid-gap states is much more prominent in the Pr interstitial case. Since such levels can promote the recombination processes of the photogenerated charge carriers, the interstitial Pr arrangement is not consistent with the estimated τ increase with respect to the dopant amount found by photocurrent measurements.

As also in the case of substitutional Pr there are new electronic levels present in the band gap, morphological aspects of the home-made samples have to be considered as well. Accordingly, at increasing the dopant amount, the specific surface areas of the powders gradually decreased. This means that less accessible

surface and a smaller amount of morphological defects, acting as possible charge carrier traps, exist in the doped samples. Also the τ estimates are found to be higher, therefore suggesting a lower importance of the recombination processes.

Eventually we remark that the uncommon combination of theoretical DFT calculations and electrochemical measurements has led to a deeper insight into the electronic and structural properties of Pr-doped titania semiconductors, determining the importance of Pr f orbitals for the increased visible absorption spectra.

Supporting Information Available: Examples of hysteresis loops obtained by BET analysis; Rietveld least-squares refinements performed on the XRPD data; the complete list of agreement factors of the various fittings; cell parameters of both the anatase and brookite phases, besides the brookite content, as a function of Pr doping; the average volume-weighted crystallite domain size, and the two different root mean square strain estimates, based on a lognormal distribution of the crystallite size. This material is available free of charge via the Internet at http://pubs.acs.org

REFERENCES

[1] Emeline, A. V.; Kuznetsov, V. N.; Rybchuk, V. K.; Serpone, N. Int. J. Photoen. 2008, 2008, 1–19.

[2] Ardizzone, S.; Cappelletti, G.; Meroni, D.; Spadavecchia F. Chem. Commun. 2011, 47, 2640–2642.

[3] Colombo, A.; Cappelletti, G.; Ardizzone, S.; Biraghi, I.; Bianchi, C. L.; Meroni, D.; Pirola, C.; Spadavecchia, F. Environ. Chem. Lett. 2012, 10, 55–60.

[4] Chen, X.; Mao, S. S. Chem. Rev. 2007, 107, 2891−2959.

[5] Huang, S. Y.; Schlichthoerl, G.; Nozik, A. J.; Graetzel, M.; Halme, J.; Boschloo, G.; Hagfeldt, A.; Lund, P. J. Phys. Chem. C 2008, 112, 5623-5637.

[6] Unger, E. L.; Ripaud, E.; Leriche, P.; Cravino, A.; Roncali, J.; Johansson, E. M. J.; Hagfeldt, A.; Boschloo, G. J. Phys. Chem. C 2010, 114, 11659–11664.

[7] Shim Y.-S.; Moon H. G.; Kim D. H; Jang, H. W.; Kang, C.-Y.; Yoon, Y.-S. Sens. Actuators B: Chem. 2011, 160, 357-363.

[8] Zhang, Z.; Lu, D.-F.; Qi, Z.-M. J. Phys. Chem. C 2012, 116, 3342-3348.

[9] Matsumoto, Y.; Murakami, M.; Hasegawa, T.; Fukumura, T.; Kawasaki, M.; Ahmet, P.; Nakajima, K.; Chikyow, T.; Koinuma, H. Appl. Surf. Sci. 2002, 189, 344-348.

[10] Hong, N. H.; Sakai, J.; Hassini, A. Appl. Phys. Lett. 2004, 84, 2602-2604.

[11] Choi, W.; Termin, A.; Hoffmann, M. R. J. Phys. Chem. 1994, 98, 13669–13679.

[12] Su, Y. L.; Zhang, X. W.; Zhou, M. H.; Han, S.; Lei, L. C. J. Photochem. Photobiol. A 2008, 194, 152–160.

[13] Gai, Y. Q.; Li, J. B.; Li, S. S; Xia, J. B.; Wei, S. H. Phys. Rev. Lett. 2009, 102, 036402–036404.

[14] Liang, C.; Liu, C.; Li, F.; Wu, F. Chem. Eng. J. 2009, 147, 219–225.

[15] Yang, J.; Dai, J.; Li, J. Appl. Surf. Sci. 2011, 257, 8965–8973.

[16] Bingham, S.; Daoud, W. A. J. Mater. Chem. 2011, 21, 2041–2050.

[17] Sibu, C. P.; Kumar, S. R.; Mukundan, P.; Warrier, K. G. K. Chem. Mater. 2002, 14, 2876–2881.

[18] Zhang, H. X.; Xu, Y. X.; Wang, Y. G. J. Solid State Chem. 2004, 177, 3490–3498.

[19] Li, F. B.; Li, X. Z.; Ng, K. H. Ind. Eng. Chem. Res. 2006, 45, 1–7.

[20] Parida, K. M.; Sahu, N. J. Mol. Catal. A: Chem. 2008, 287, 151–158.

[21] Li, J. H.; Yang, X.; Yu, X. D.; Xu, L. L.; Kang, W. L.; Yan, W. H.; Gao, H. F.; Liu, Z. H. ; Guo, Y. H. Appl. Surf. Sci. 2009, 255, 3731–3738.

[22] Wang, Y.; Cheng, H.; Zhang, L.; Hao, Y.; Ma, J.; Xu, B.; Li, W. J. Mol. Catal. A: Chem. 2000, 151, 205–216.

[23] Xu, A.-W.; Gao, Y.; Liu, H.-Q. J. Catal. 2002, 207, 151–157.

[24] Da Silva, J. L. F., Ganduglia-Pirovano, M. V.; Sauer, J.; Bayer, V.; Kresse, G. Phys. Rev. B 2007, 75, 045121/1–045121/10.

[25] Chen, W.; Yuan, P.; Zhang, S.; Sun, Q.; Liang, E.; Jia, Y. Physica B: Cond. Mat. 2012, 407, 1038–1043.

[26] Ceotto, M.; Lo Presti, L.; Cappelletti, G.; Meroni, D.; Spadavecchia, F.; Zecca, R.; Leoni, M.; Scardi, P.; Bianchi, C. L.; Ardizzone, S. J. Phys. Chem. C 2012, 116, 1764–1771.

[27] Larson, A. C.; Von Dreele, R. B. General Structural Analysis System (GSAS); Los Alamos National Laboratory Report, LAUR 86, 2004.

[28] Toby, B. H. J. Appl. Cryst., 2001, 34, 210-213.

[29] Pitschke, W.; Hermann, H.; Mattern, N. Powder Diffraction, 1993, 8, 74-83.

[30] Thompson, P.; Cox, D. E.; Hastings, J. B. J. Appl. Crist., 1987, 20, 79-83.

[31] Bunge, H. J. Texture Anal. Mat. Sci.; Butterworth-Heinemann, Oxford, 1983; Von Dreele, B. J. Appl. Cryst., 1997, 30, 517-525.

[32] Fernandez-Gonzalez, R.; Julian-Lopez, B.; Purificacion Escribano, E. C. J. Mater. Chem., 2011, 21, 497–504.

[33] Hagfeldt, A.; Lindström, H.; Södergren, S.; Linquist, S.-E. J. Elecroanal. Chem. 1995, 381, 39–46.

[34] Roy, A. M.; De, G. C.; Sasmal, N.; Bhattacharyya, S. S. Int. J. Hydrogen Energy 1995, 20, 627–630.

[35] Spadavecchia, F.; Cappelletti, G.; Ardizzone, S.; Ceotto, M.; Falciola, L. J. Phys. Chem. C 2011, 115, 6381–6391.

[36] Perdew, J. P.; Burke, K.; Ernzerhof, M. Phys. Rev. B 1996, 54, 16533-16539.

[37] Hohenberg, P.; Kohn, W. Phys. Rev. 1964, 136, B864-B871.

[38] Kohn, W.; Sham, L. J. Phys. Rev. 1965, 140, A1133–A1138.

[39] Perdew, J. P.; Wang, Y. Phys. Rev. B 1992, 45, 13244–13249.

[40] Perdew, J. P.; Burke, K.; Ernzerhof, M. Phys. Rev. Lett. 1996, 77, 3865–3868.

[41] Bhöchl, P. E. Phys. Rev. B 1994, 50, 17953–17979.

[42] Kresse, G.; Joubert, D. Phys. Rev. B 1999, 59, 1758–1775.

[43] Kresse, G.; Hafner, J. J. Phys. Rev. B, 1993, 47, 558–561.

[44] Kresse, G.; Furthmüller, J. Phys. Rev. B 1996, 54, 11169–11186.

[45] Harris, J. Phys. Rev. B 1985, 31, 1770–1779.

[46] Foulkes, W. M. C.; Haydock, T. Phys. Rev. B 1989, 39, 12520–12536.

[47] Teter, M. P.; Payne, M. C.; Allan, D. C. Phys. Rev. B 1989, 40, 12255–12263.

[48] Bylander, D. M.; Kleinman, L.; Lee, S. Phys Rev. B 1990, 42, 1394–1403.

[49] Davidson, E. R. in Methods in Computational Molecular Physics; Dierksen, G. H. F., Ed.; NATO Advanced Study Institute, Series C; Plenum: New York, NY, 1983; Vol. 113, p. 95.

[50] Dudarev, S. L.; Botton, C. A.; Savarsov, S. Y.; Hunphreys, C. J.; Sutton, A. P. Phys. Rev. B 1998, 57, 1505–1509.

[51] Nolan, M.; Elliott, S. D.; Mulley, J. S.; Bennett, R. A.; Basham, M.; Mulheran, P. Phys. Rev. B 2008, 77, 14–18.

[52] Poteryaev, A. I.; Lichtenstein, A. I.; Kotliar, G. Phys. Rev. Lett. 2004, 93, 086401/1–086401/4.

[53] Pentcheva, R.; Pickett, W. E. Phys. Rev. B 2006, 74, 035112/1–035112/7.

[54] Cuong, D. D.; Lee, B.; Choi, K. M.; Ahn, H. S.; Han, S.; Lee, J. Phys. Rev. Lett. 2007, 98, 115503/1–115503/4.

[55] Morgan, B. J.; Watson, G. W. Surf. Sci. 2007, 601, 5034–5041.

[56] Calzado, C. J.; Hernández, N. C.; Sanz, J. F. Phys. Rev. B 2008, 77, 045118/1–045118/10.

[57] Hu, Z.; Metiu, H. J. Phys. Chem. C 2011, 115, 5841–5845.

[58] Cococcioni, M.; De Gironcoli, S. Phys. Rev. B 2005, 71, 035105/1–035105/16.

[59] Kulik, H. J.; Cococcioni, M.; Scherlis, D. A.; Marzari, N. Phys. Rev. Lett. 2006, 97, 103001/1–103001/4.

[60] Mattioli, G.; Alippi, P.; Filippone, F.; Caminiti, R.; Amore Bonapasta, R. J. Phys. Chem. C 2010, 114, 21694–21704.

[61] Kowalski, P. M.; Camellone, M. F.; Nair, N. N.; Meyer, B.; Marx, D. Phys. Rev. Lett. 2010, 105, 146405/1–146405/4.

[62] Rubio-Ponce, A.; Conde-Gallardo, A.; D. Olguin, A. Phys. Rev. B 2008, 78, 035107/1–03517/9.

[63] Zhao, Z. Y.; Liu, Q. J.; J. Phys. D: Appl. Phys 2008, 41, 085417/1–08541/9.

[64] Adachi, G.; Imanaka, N. Chem. Rev. 1998, 98, 1479–1514.

[65] Osten, H. J.; Bugiel, E.; Dabrowski, J.; Fissel, A.; Guminskaya, T.; Liu, J. P.; Mussig, H. J.; Zaumseil, P. Gate Insulator, IWGI, Tokyo, 2001, p. 100.

[66] Burdett, J. K.; Hughbandks, T.; Miller, G. J.; Richardson, J. W.; Smith, J. V. J. Am. Chem. Soc. 1987, 10, 3639–3646.

[67] Bickley, R. I.; Gonzales-Carreno, T.; Lees, J. S.; Palmisano, L.; Tilley, R. J. D.; J. Solid State Chem. 1991, 92, 178–190.

[68] Yana, X.; Hea, J.; Evans, D. G.; Duana, X.; Zhub, Y. Appl. Cat. B: Environ. 2005, 55, 243–252.

[69] Gonschorek, W. Z. Kristallogr. 1982, 160, 187–203.

[70] Greis, O.; Ziel, R.; Breidenstein, B.; Haase, A.; Petzel, T. J. Alloys and Compounds, 1994, 216, 255–258.

[71] Kolitsch, U.; Seifert, H. J.; Aldinger, F. J. Solid State Chem. 1995, 120, 38–42.

[72] Ranjit, K. T.; Willner, I.; Bossmann, S. H.; Braun, A. M. Environ. Sci. Technol. 2001, 35, 1544–1549.

[73] Amlouk, A.; El Mir, L.; Kraiem, S.; Saadoun, M.; Alaya, S.; Pierre, A. C. Mat. Sci. Eng B 2008, 146, 74–79.

[74] Meneghini, C.; Dalconi, M. C.; Nuzzo, S.; Mobilio, S.; Wenk, R. H. Biophys. J. 2003, 84, 2021–2029.

[75] Williamson, G. K.; Hall, W. H. Acta Metall. 1951, 1, 22–31.

[76] Balzar, D.; Ledbetter, H. J. Appl. Cryst. 1993, 26, 97–103.

[77] Balzar, D. Voigt-function model in diffraction line-broadening analysis, in Microstructure Analysis by Diffraction, R. L. Snyder, J. Fiala, H. J. Bunge, IUCr series, Oxford University Press, 2000.

[78] Balzar, D. J. Appl. Cryst., 1995, 28, 244–245.

[79] Balzar, D. J. Appl. Cryst. 1992, 25, 559–570.

[80] Langford, J. I. Crystallite Size from Diffraction Data; in Newsletter No. 24, Commission of Powder Diffraction, IUCr, 2000.

[81] Shannon, R. D. Acta Cryst. 1976, A32, 751–767.

[82] Li, F. B.; Li, X. Z.; Cheah, K. W.; Environ. Chem. 2005, 2, 130–137.

[83] Spadavecchia, F.; Cappelletti, G.; Ardizzone, S.; Bianchi, C. L.; Cappelli, S.; Oliva, C.; Scardi, P.; Leoni, M.; Fermo, P. Appl. Catal., B 2010, 96, 314–322.

[84] Dholam, R.; Patel, N.; Santini, A.: Miotello, A. Int. J. Hydrogen Energy 2010, 35, 9581–9590.

[85] Radecka, M.; Rekas, M.; Trenczek-Zajac, A.; Zakrzewska, K J. Power Sources 2008, 181, 46–55.

[86] Tafalla, D.; Salvador, P.; Benito, R. M. J. Electrochem. Soc. 1990, 137, 1810–1815.

[87] B. O'Regan, J. Moser, M. Anderson, M. Grätzel J. Phys. Chem. 1990, 94,8720–8726.

[88] Byrne, J. A.; Eggins, B.R. J. Electroanal. Chem. 1998, 457, 61–72.

[89] Krýsa, J.; Zlamal, M.; Waldner, G. J. Appl. Electrochem. 2007, 37, 1313–1319.

TABLES

Table 1. Specific surface areas, pore volumes (BET-BJH analysis) and quasi-Fermi levels (photovoltage method).† The standard deviation is 0.2 V for all samples.

Sample	S_{BET} (m$_2$ g$_{-1}$)	Total pore volume (mL g$_{-1}$)	d< 6 nm pores (%)	6-80 nm pores (%)	> 80 nm pores (%)	E_f^{n}* (V vs NHE) †
T	160	0.34	64	27	9	-0.67
TPr_0.2	108	0.17	86	12	2	-0.65
TPr_0.3	102	0.15	90	8	2	-0.64
TPr_0.5	111	0.15	91	7	2	-0.59
TPr_0.7	118	0.16	91	7	2	-0.62

FIGURE CAPTIONS

Figure 1. HRTEM images of undoped (a), 0.2% (b) and 0.5% (c) Pr-doped TiO_2 particles.

Figure 2. Color online. Collected powder patterns (blue crosses), with the corresponding least-square fitting curve and the y_{obs}-y_{calc} point-by-point difference (red lines). The computed angular positions of both anatase and brookite reflections in pure TiO_2 are marked at the bottom of the plot.

Figure 3. Behavior of some reflection-broadening parameters as a function of the Pr doping extent. (a) Full-width at half maximum (FWHM) of some low-angle reflections belonging to the anatase structure, as computed from the least-squares optimized profile coefficients in GSAS. The plotted curves serve as eye guidelines. (b) Volume-weighted average crystallite dimensions, D_V (blue squares, left axis) and average lattice strain, Σ (red triangles, right axis), as computed from the Williamson-Hall method for the anatase reflections below $2\vartheta=60°$. The plotted curves serve as eye guidelines. (c) Volume-weighted column-length distribution, normalized on unit volume, of the anatase crystallites along the real vector modulus (L) orthogonal to the anatase (101) plane family, as computed from the double-Voigt method assuming a lognormal distribution of the crystallites. (d) Same as (c), for the lattice strain distribution estimated from the double-Voigt method. The error bars, when present, correspond to ±1 estimated standard deviations (esd's).

Figure 4. Averaged distortion d parameter of the primitive cell. Different colors and symbols for difference U values.

Figure 5. Diffuse reflectance spectra of the undoped (T) and all Pr-doped samples.

Figure 6. Electronic density of states (DOS) for substitutional (left column) and interstitial (right column) Pr doping of anatase TiO_2. Comparison between different U values on each panel. Continuous black and dashed red lines for the oxygen defected Pr doped TiO_2 spin-polarized calculation, continuous green line for Pr 4d orbitals and continous blue line for Pr 4f orbitals. The Pr 4d and 4f DOS has been magnified 10 times for convenience. The Fermi energy is indicated by the vertical dashed lines.

Figure 7. (a) Photocurrent transient curve for a selected sample (TPr_0.3). (b) Normalized plot of current-time dependence for the same doped sample compared to the undoped one; inset: table with the transient time constants for all samples irradiated by UV light. ‡ The τ standard deviation is 2 ∫ for all samples.

Figure 1

Figure 2
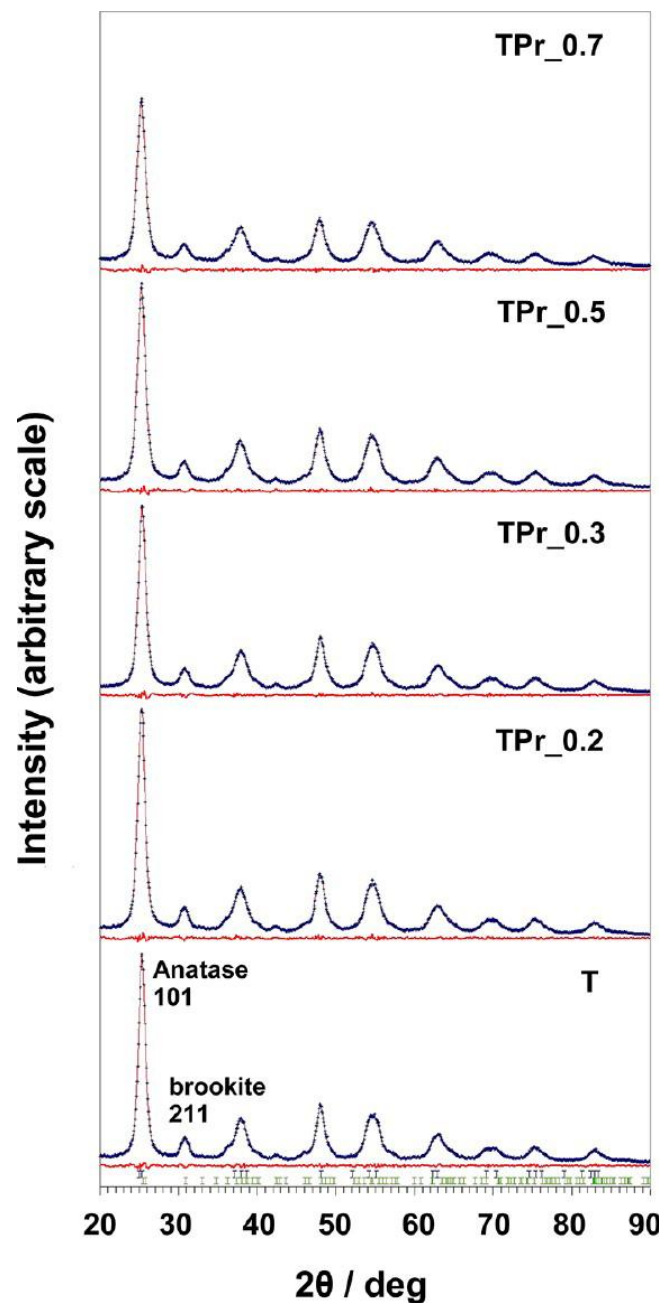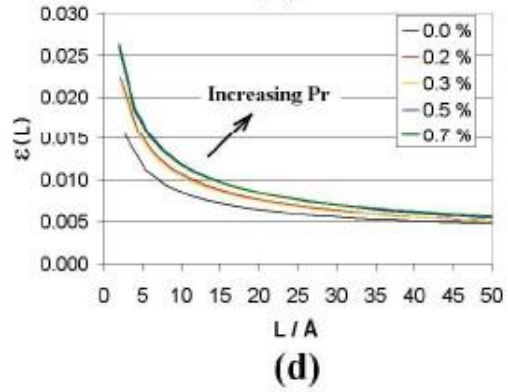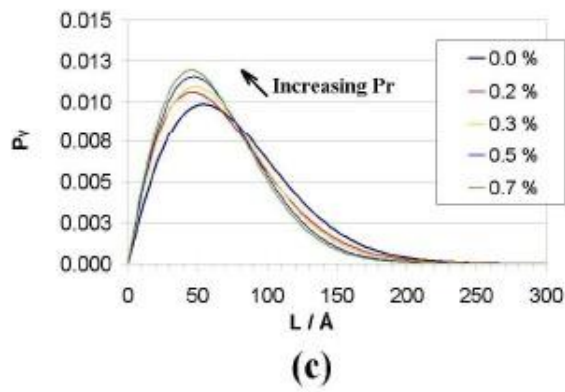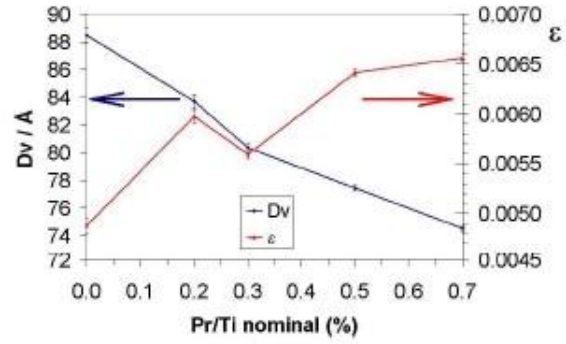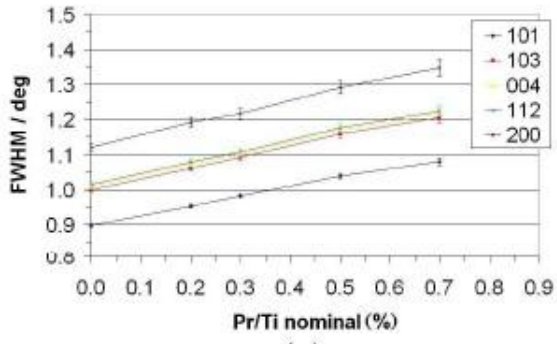
Figure 3

(a)

(b)

(c)

(d)
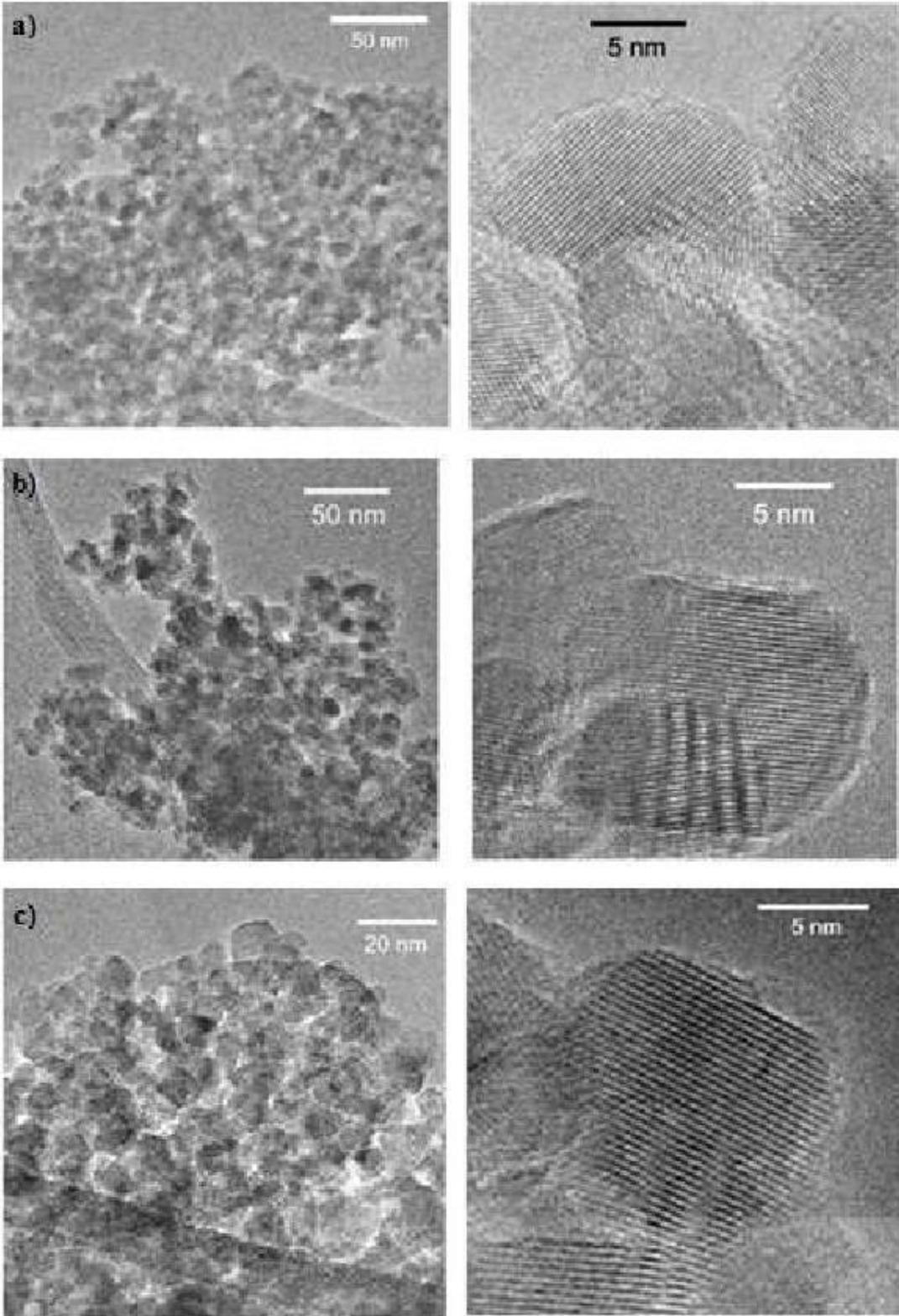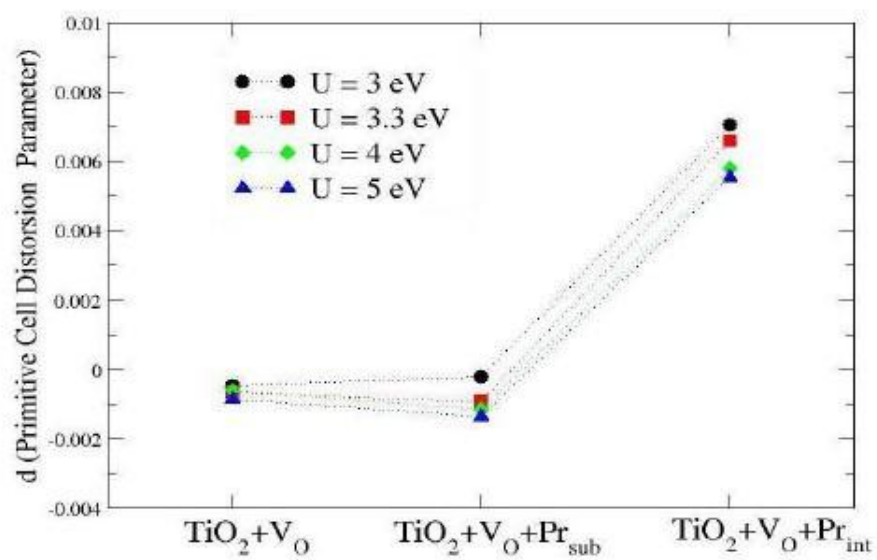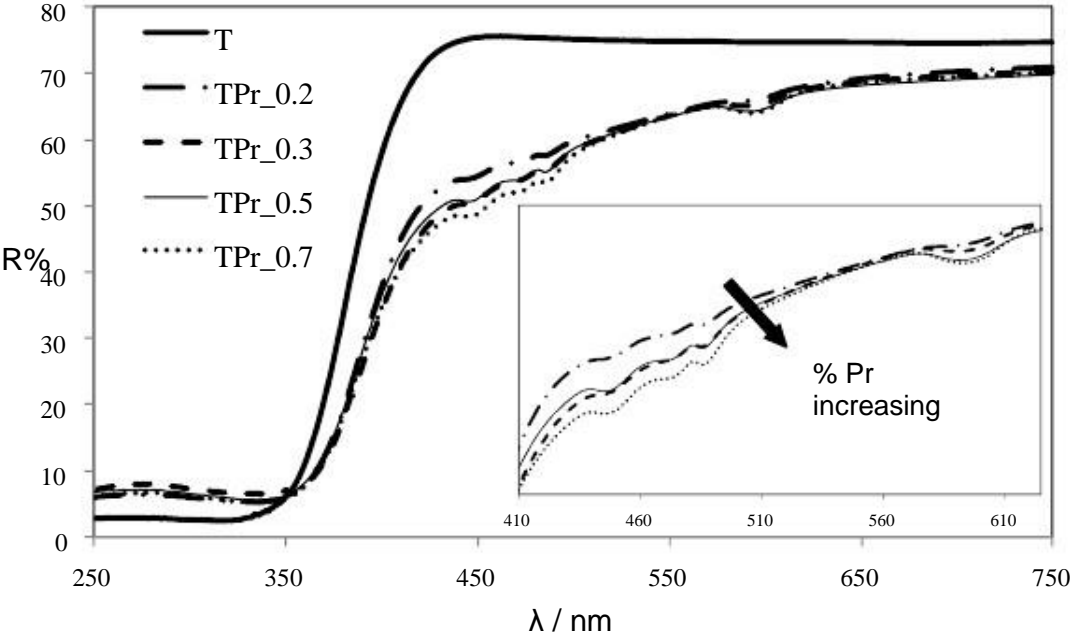
Figure 4

Figure 5

Figure 6
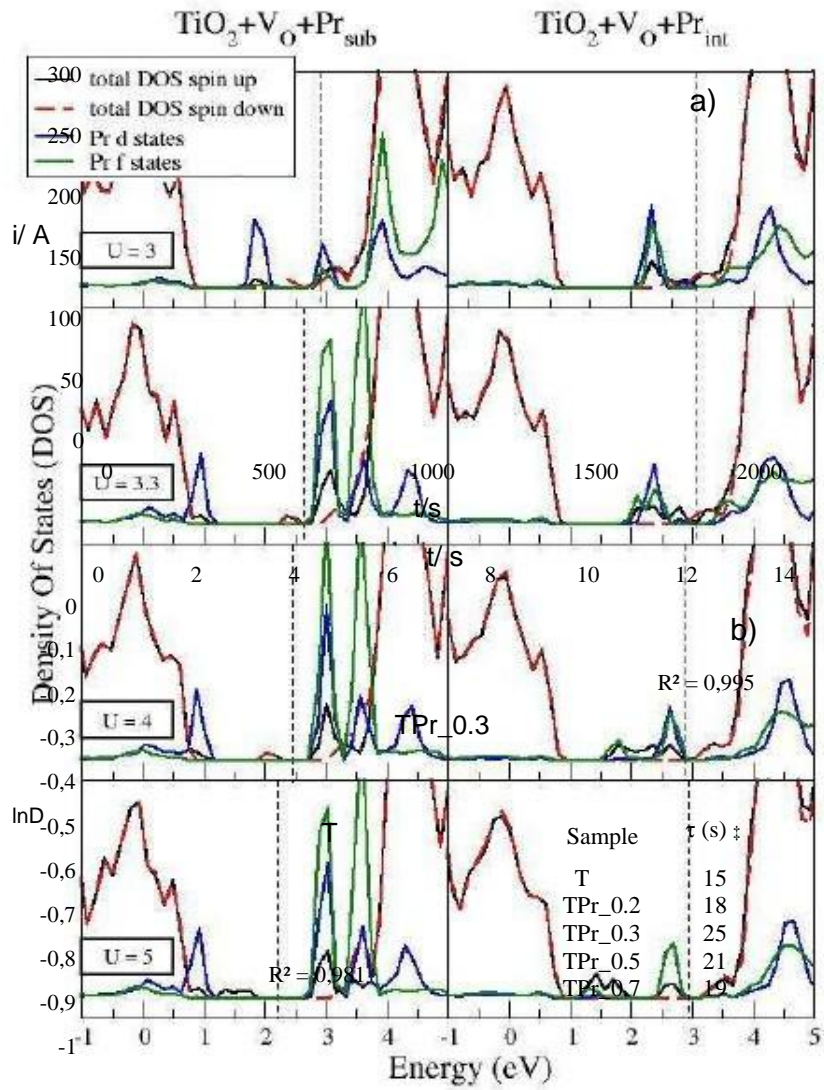
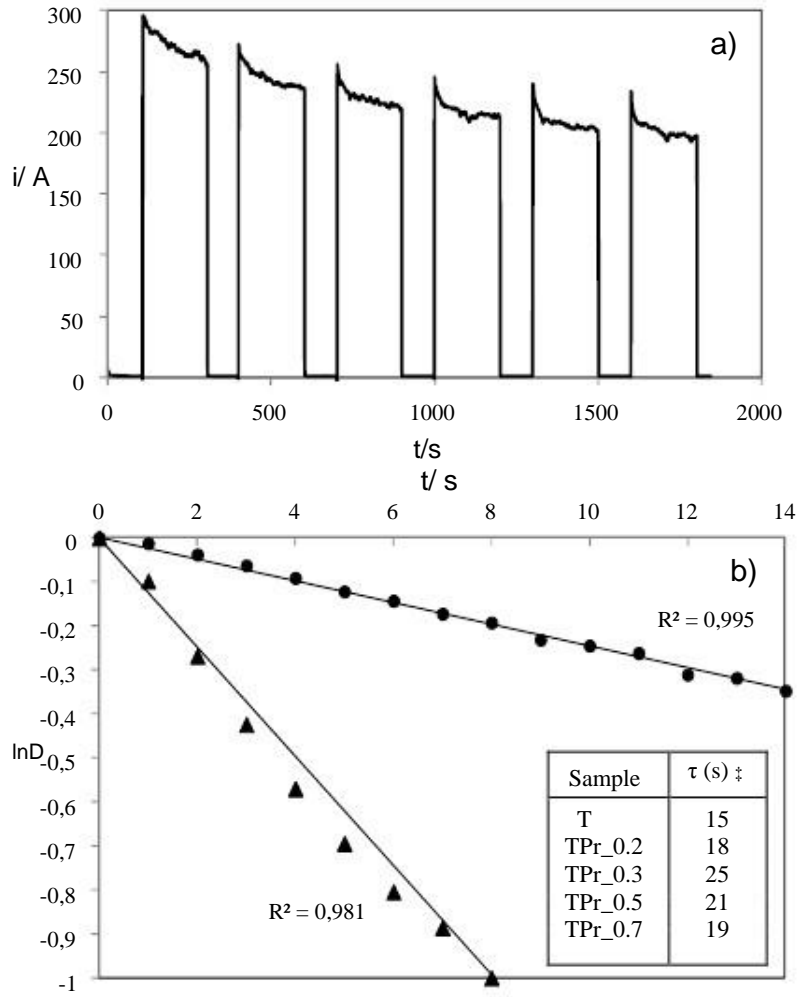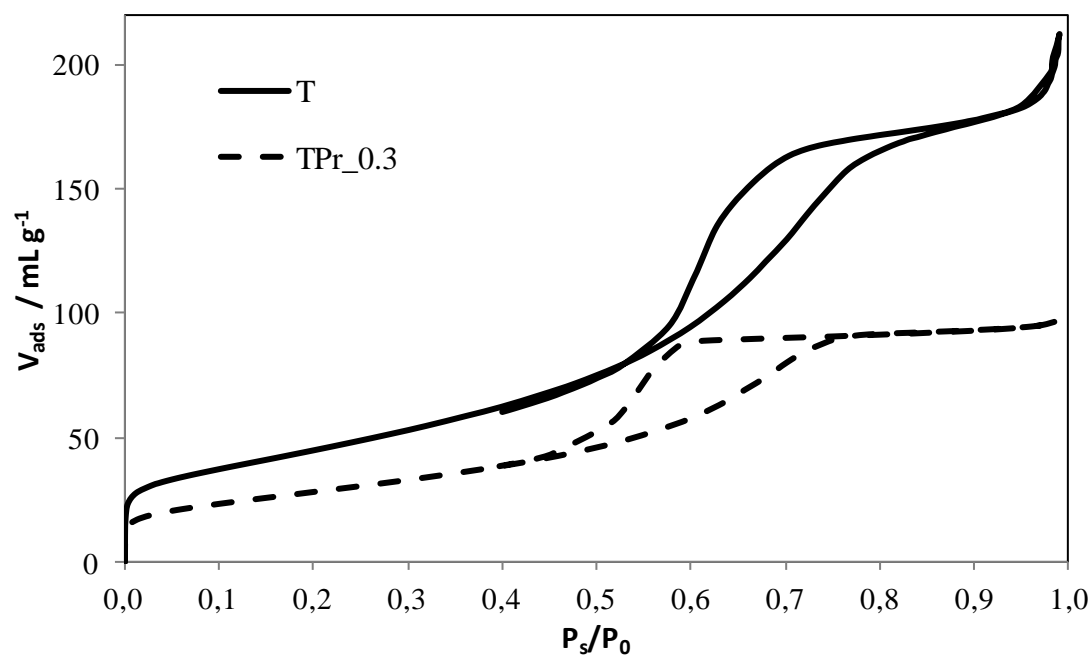Figure 7

Figure S1. Hysteresis loops of the undoped sample (T) and a doped one (TPr_0.3) as representative cases, obtained by BET analysis.

Table S1. Background-subtracted agreement factors and statistical indices[1] for the Rietveld least-squares refinements performed on the XRPD data collected in this work.

Nominal Pr/Ti content (%)	0.00	0.2	0.3	0.5	0.7
R_{wp} [a]	0.034	0.031	0.031	0.029	0.030
χ^2 [b]	1.596	1.425	1.322	1.351	1.277
D_{wd} [c]	1.623	1.435	1.513	1.481	1.753
R_p [d]	0.027	0.025	0.025	0.023	0.025
$R(F^2)$ [e]	0.013	0.011	0.012	0.011	0.030

Table S2. Structural model (dimensionless relevant atomic fractional coordinates and isotropic thermal parameters x 100, Å^2) for the anatase and brookite phases in the nanocrystalline samples here considered, as retrieved for the Rietveld refinement. See Table S3 for the corresponding cell parameters.

Anatase (Ti: 0 1/4 3/8; O: 0 1/4, z)

Nominal Pr/Ti content (%)	O(z)	U (Ti)	U(O)
0.0	0.16898(29)	2.3(1)	3.1(1)
0.2	0.16915(28)	2.3(1)	3.1(1)
0.3	0.16938(29)	2.3(1)	3.2(2)
0.5	0.16911(27)	2.2(1)	3.3(1)
0.7	0.17003(31)	2.2(1)	3.5(1)

---

[a] Weighted profile R-factor, defined as $R_{wp} = \sqrt{\dfrac{\sum w_i \cdot \left(y_i^{obs} - y_i^{calc}\right)^2}{\sum w_i \cdot \left(y_i^{obs}\right)^2}}$, where w_i are the statistical weights and y_i the observed and computed intensities at the ith-step of the diffraction profile.

[b] Goodness-of-fit (reduced χ^2), defined as $\chi^2 = \dfrac{\sum w_i \cdot \left(y_i^{obs} - y_i^{calc}\right)^2}{N_{obs} - N_{par}}$, N_{obs} and N_{par} being the number of profile points and the number of least-square parameters employed in the model, respectively.

[c] Durbin-Watson[2] estimate of the serial correlation in the powder diffraction pattern. It is defined as $D_{wd} = \dfrac{\sum \left(\Delta_i / \sigma_i - \Delta_{i-1} / \sigma_{i-1}\right)^2}{\sum \left(\Delta_i / \sigma_i\right)^2}$, where Δ_i are the y^{obs}-y^{calc} differences and σ_i the corresponding standard deviation for the observed intensity at the ith step of the profile. The closer to 2 is D_{wd}, the less correlated are the least-square parameters.

[d] Unweighted profile-R factor, defined as $R_p = \dfrac{\sum y_i^{obs} - y_i^{calc}}{\sum y_i^{obs}}$.

[e] Agreement factor for the extracted squared structure factor amplitudes (F^2) values. It is reported here for the sake of completeness, as this quantity is *not* minimized during the Rietveld least-square optimization.

Brookite

Nominal Pr/Ti content (%)	Ti (x, y, z)	O1 (x, y, z)	O2 (x, y, z)	U(Ti)	U(O1, O2)
0.0	0.1326(5) 0.0953(6) 0.8619(7)	0.0142(12) 0.1589(18) 0.1978(22)	0.2212(15) 0.1302(26) 0.5226(18)	2.9(1)	2.9(2)
0.2	0.1336(4) 0.0943(5) 0.8624(7)	0.0104(11) 0.1641(17) 0.2039(22)	0.2211(14) 0.1333(22) 0.5256(18)	3.1(1)	3.4(2)
0.3	0.1336(4) 0.0941(6) 0.8631(7)	0.0096(12) 0.1659(18) 0.2067(21)	0.2195(14) 0.1297(25) 0.5263(18)	3.1(1)	3.0(2)
0.5	0.1349(4) 0.0937(6) 0.8627(7)	0.0060(13) 0.1667(18) 0.2106(20)	0.2222(13) 0.1279(24) 0.5197(19)	3.6(1)	2.6(2)
0.7	0.1374(4) 0.0937(6) 0.8630(8)	0.0071(13) 0.1695(17) 0.2120(21)	0.2273(11) 0.1231(22) 0.5213(21)	3.9(1)	2.0(2)

Table S3. XRPD anatase ($I4_1/amd$) and brookite (Pbca) symmetry-independent lattice parameters (Å) and unit cell volumes (Å^3) as a function of the Pr doping extent. Estimated standard deviations (esd's) from the Rietveld fitting are given in parentheses.

Anatase

Nominal Pr/Ti content (%)	0.0	0.2	0.3	0.5	0.7
a	3.7850(2)	3.7847(2)	3.7849(2)	3.7844(2)	3.7848(2)
c	9.473(1)	9.475(1)	9.471(1)	9.472(1)	9.471(2)
V	135.72(2)	135.73(2)	135.68(2)	135.65(3)	135.67(3)

Brookite

Nominal Pr/Ti content (%)	0.0	0.2	0.3	0.5	0.7

a	9.151(3)	9.156(3)	9.145(3)	9.166(4)	9.154(4)
b	5.439(2)	5.439(2)	5.439(2)	5.437(2)	5.436(2)
c	5.161(2)	5.166(2)	5.173(2)	5.166(2)	5.173(2)
V	256.84(14)	257.26(14)	257.31(14)	257.46(16)	257.42(17)

Table S4. Weight fractions of anatase and brookite phases as a function of the Pr doping extent, as retrieved from the Rietveld refinement on the XRPD data. Estimated standard deviations (esd's) are given in parentheses.

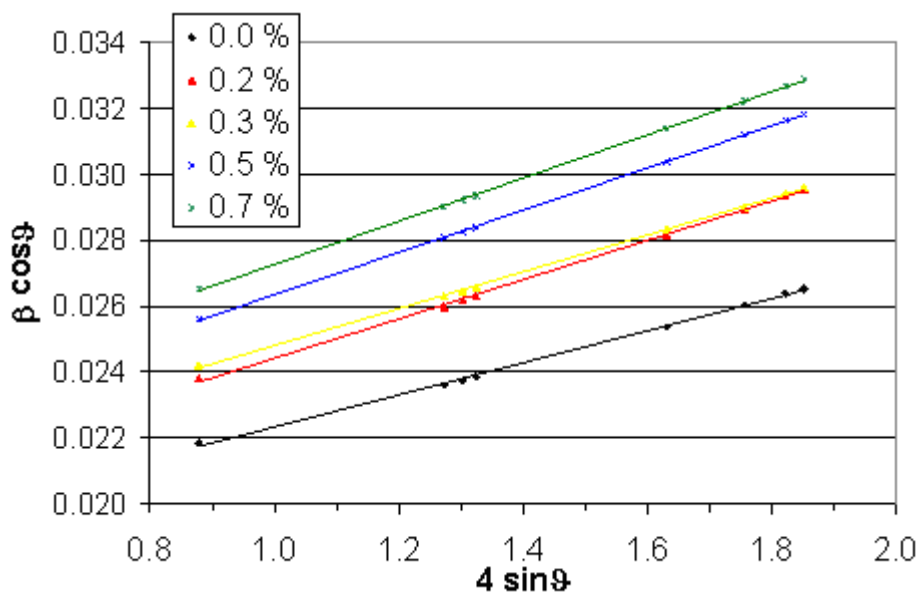| Nominal Pr/Ti content (%)	0.0	0.2	0.3	0.5	0.7
Anatase	0.614(1)	0.612(1)	0.613(1)	0.611(1)	0.610(1)
Brookite	0.386(2)	0.388(2)	0.387(2)	0.389(2)	0.390(2)

Figure S2. Williamson-Hall least-squares plots for the 8 anatase reflections with $2\vartheta < 60$. The observed integral breadth values β were computed by the program BREADTH[3] from the corresponding full-width at half maximum estimates corrected for the instrumental broadening contribution.

Table S5. Least-squares parameters and correlation coefficients R^2 of the Williamson-Hall curves (in the form $y = mx + q$) shown in Figure S2.

Nominal Pr/Ti content (%)	m	q	R^2

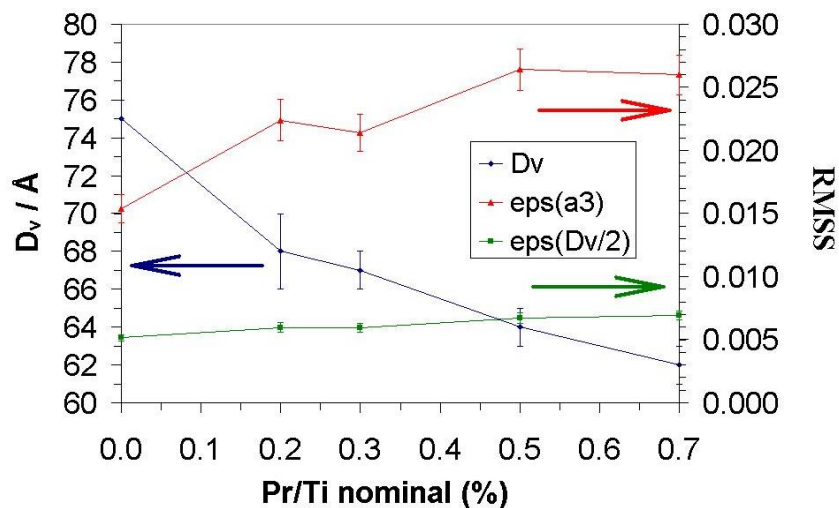|			
0.0	0.00488(7)	0.0174(1)	0.9987
0.2	0.00597(7)	0.0184(1)	0.9991
0.3	0.00559(5)	0.0192(1)	0.9995
0.5	0.00641(3)	0.0199(1)	0.9998
0.7	0.00656(4)	0.0207(1)	0.9998

Figure S3. Outcomes of the double-Voigt method for size-strain estimates, referred to the anatase lattice, as a function of the Pr doping extent. The plotted parameters come from the program BREADTH[3] applied to three reflections of increasing order belonging to the (101) family, i.e. (101), (202) and (303) (see the main text). The dark blue points (left axis) refer to the average volume-weighted crystallite domain size, D_V. The red triangles and the green squares (right axis) show the behavior of two different root mean square strain estimates, RMSS ($<\varepsilon^2>^{1/2}$), averaged over the a_3 (the edge of the orthorhombic cell, orthogonal to the diffracting planes) or the $D_V/2$ real distances.

Table S6. Nearest oxygen atoms from substitutional center (distances in Å).

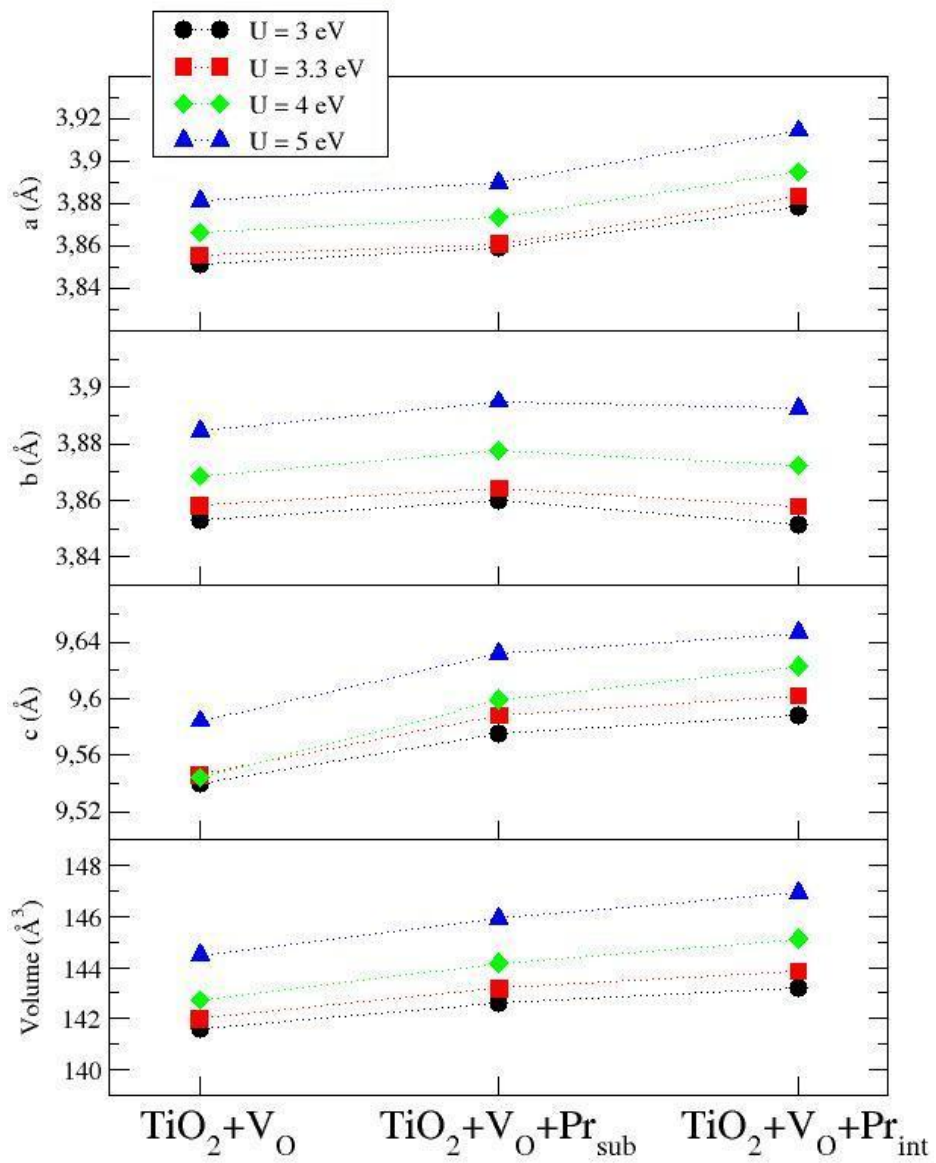| U values for Ti	System	R(X-1)	R(X-2)	R(X-3)	R(X-4)	R(X-5)	R(X-6)
$3 - 3.3 - 4 - 5$	X = Ti	1.97	1.97	2.00	2.00	1.97	1.97
3	X = Pr	2.15	2.15	2.29	2.27	2.15	2.14
3.3	X = Pr	2.13	2.13	2.22	2.23	2.12	2.12
4	X = Pr	2.13	2.13	2.22	2.22	2.13	2.13
5	X = Pr	2.13	2.13	2.22	2.22	2.13	2.13

Figure S4. Primitive cell parameters (a,b,c) and cell volume variation under Pr doping and for different values of U.
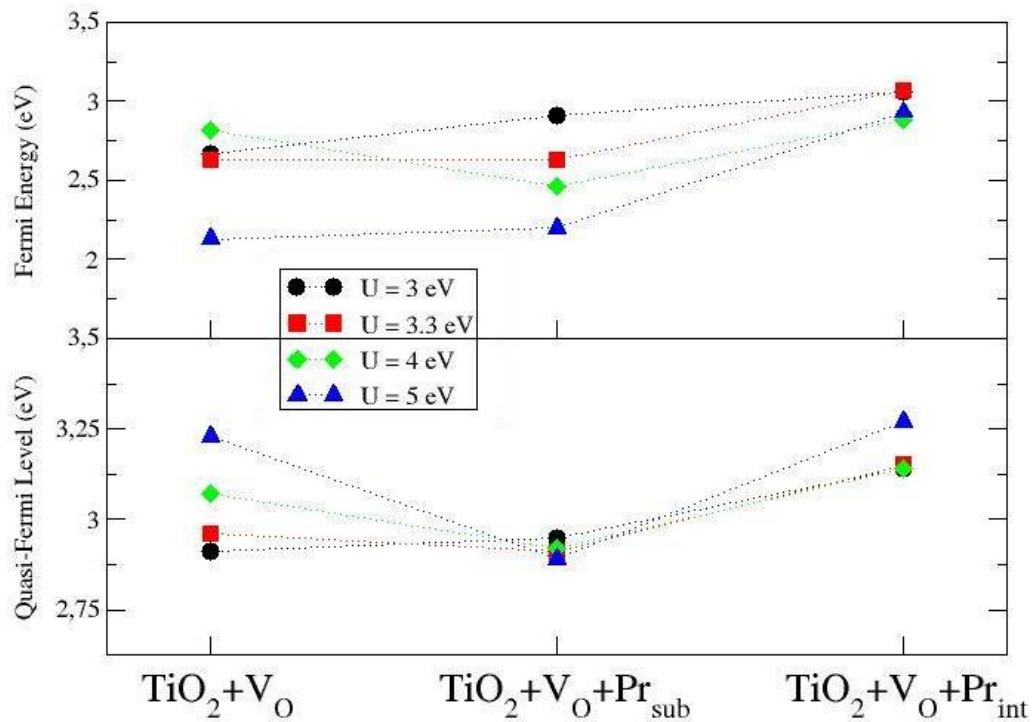
Figure S5. Fermi and quasi-Fermi energies for different Pr doping and for different values of U. Upper panel: there is not a clear trend for the Fermi energy variation for all U values. However, an interstitial Pr doping is seen to shift the Fermi level toward the conduction band. Lower panel: the quasi-Fermi energy levels are raised toward the conduction band only the interstitial doping.

[1] Larson, A. C.; Von Dreele, R. B. *General Structural Analysis System (GSAS)*; Los Alamos National Laboratory Report, LAUR 86, 2004.

[2] Durbin, J.; Watson, G. S. *Biometrika*, **1971,** *58*, 1-19.

[3] Balzar, D. *J. Appl. Cryst.*, **1995**, *28*, 244-245.